

# Deciphering the Origin of the GeV-TeV Gamma-Ray Emission from SS 433

Shigeo S. Kimura<sup>1,2</sup>, Kohta Murase<sup>3,4,5,6</sup>, and Peter Mészáros<sup>3,4,5</sup>

Frontier Research Institute for Interdisciplinary Sciences, Tohoku University, Sendai 980-8578, Japan

Astronomical Institute, Tohoku University, Sendai 980-8578, Japan

Department of Physics, The Pennsylvania State University, University Park, PA 16802, USA

Department of Astronomy & Astrophysics, The Pennsylvania State University, University Park, PA 16802, USA

Center for Multimessenger Astrophysics, Institute for Gravitation and the Cosmos, The Pennsylvania State University, University Park, PA 16802, USA

Center for Gravitational Physics, Yukawa Institute for Theoretical Physics, Kyoto, Kyoto 606-8502, Japan

Received 2020 August 11; revised 2020 September 20; accepted 2020 October 2; published 2020 December 3

#### Abstract

We investigate hadronic and leptonic scenarios for the GeV–TeV gamma-ray emission from jets of the microquasar SS 433. The emission region of the TeV photons coincides with the X-ray knots, where electrons are efficiently accelerated. On the other hand, the optical high-density filaments are also located close to the X-ray knots, which may support a hadronic scenario. We calculate multiwavelength photon spectra of the extended jet region by solving the transport equations for the electrons and protons. We find that both hadronic and leptonic models can account for the observational data, including the latest Fermi Large Area Telescope result. The hadronic scenarios predict higher-energy photons than the leptonic scenarios, and future observations such as with the Cherenkov Telescope Array, the Large High-Altitude Air Shower Observatory, and the Southern Wide-field Gamma-ray Observatory may distinguish between these scenarios and unravel the emission mechanism of GeV–TeV gamma rays. Based on our hadronic scenario, the analogy between microquasars and radio galaxies implies that the X-ray knot region of the radio-galaxy jets may accelerate heavy nuclei up to ultrahigh energies.

*Unified Astronomy Thesaurus concepts:* Gamma-ray astronomy (628); Jets (870); Non-thermal radiation sources (1119); Cosmic ray sources (328)

#### 1. Introduction

SS 433 is a microquasar that powers bipolar precessing jets from the central compact object (see Fabrika 2004 for a review). The central object is expected to accrete the material at a super-Eddington rate (van den Heuvel 1981). The jets are interacting with interstellar matter at tens of parsecs, creating a bright radio nebula (Dubner et al. 1998) and extended X-ray lobes (Seward et al. 1980; Watson et al. 1983; Yamauchi et al. 1994). The X-ray lobes have bright knots in both the eastern and western jets (Safi-Harb & Ögelman 1997; Safi-Harb & Petre 1999). Recently, the High Altitude Water Cherenkov (HAWC) collaboration reported 20 TeV gamma-rays associated with the X-ray knots (Abeysekara et al. 2018), which indicates the existence of particles of at least a few hundreds of TeV.

Some groups have searched for the high-energy gamma-rays from SS 433 using the Fermi Large Area Telescope (LAT), but the results differ from each other. Bordas et al. (2015) discovered a gamma-ray source at a position consistent with SS 433, but not aligned with the extended jet. Xing et al. (2019) reported detection of GeV gamma rays with a soft spectrum from the western knot but nondetection from the eastern knot. Rasul et al. (2019) discovered a periodic gamma-ray emission from the SS 433 region, and argued that the emission comes from the central object. By contrast, Sun et al. (2019) found that the GeV gamma-ray emission region is larger than the TeV gamma-ray emission region, arguing that the GeV source likely originates from W50, a radio nebula surrounding SS 433, rather than the SS 433 knots.

Recently, Fang et al. (2020) performed a joint analysis of Fermi-LAT and HAWC data, and concluded that the GeV gamma-ray data may be smoothly connected to the TeV range with a photon index  $\Gamma \sim 2.1$ . They found that the previous

Fermi-LAT analyses were affected by nearby sources, J1913.3 +0515 in the Fermi-LAT 8 yr point-source catalog and J1907.9 + 0602 in the 4FGL catalog (Abdollahi et al. 2020). Using the different point-source catalogs and response functions leads to various conclusions.

The gamma-ray emission region coincides with the X-ray knots (Safi-Harb & Ögelman 1997). It is widely believed that high-energy electrons accelerated at the knots emit X-rays by the synchrotron mechanism. Thus, most previous works focus on the leptonic scenario for the TeV gamma-ray emission mechanism (Abeysekara et al. 2018; Xing et al. 2019; Fang et al. 2020; Sudoh et al. 2020). However, hadronic emission could provide a dominant contribution for the observed gamma rays (Reynoso & Carulli 2019). Optical filaments exist within the angular uncertainty of the gamma-ray signals in the eastern lobe (Zealey et al. 1980; Konigl 1983; Boumis et al. 2007). The particle number density in the filaments is much higher than in the ambient medium, which motivates us to investigate a hadronic scenario more carefully.

In this paper, we examine both scenarios using the multiwavelength data, including the latest GeV data by Fermi-LAT, and discuss the scenario feasibility and tests by future observations. We focus on the eastern lobe. In the western lobe, it is unclear whether dense filaments exist close to the gamma-ray emission region or not, and we avoid discussion of hadronic scenario there. In Section 2, we construct a steady-state one-zone model, and describe the model parameters obtained from multiwavelength observations. Our calculation results are shown in Section 3, and the analogy to large-scale jets in radio galaxies is discussed in Section 4. We discuss the implications in Section 5 and summarize our results in Section 6. The notation of  $Q_X = Q/10^X$  in cgs unit is used unless otherwise noted.

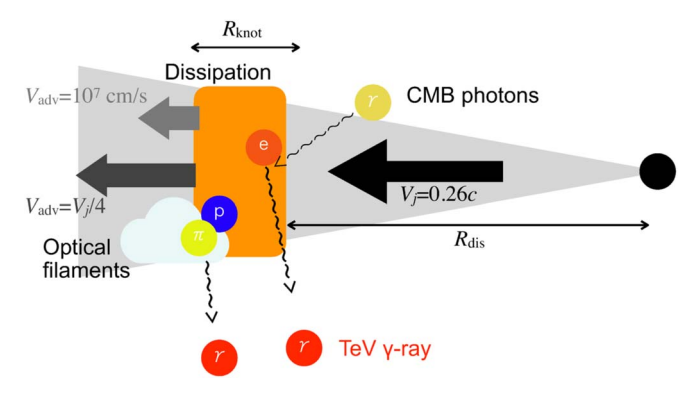


Figure 1. Schematic picture of our models. The jets dissipate their kinetic energy at a dissipation radius,  $R_{\rm dis}$ , which accelerates nonthermal particles. The nonthermal protons interact with ambient matter including the dense optical filaments, producing gamma rays through pion decay. The nonthermal electrons emit gamma rays by upscattering the CMB photons. We write the size of the emission region as  $R_{\rm knot}$ . We consider four scenarios: combinations of hadronic-dominated/leptonic-dominated and fast (dark gray)/slow (light gray) advection velocity (see Table 1).

#### 2. Models

# 2.1. Formulation

We assume that the jets of kinetic luminosity  $L_j$  dissipate some of their energy at the X-ray knot, resulting in acceleration of nonthermal particles (see Figure 1 for a schematic picture). To obtain the particle spectra at the X-ray knot, we solve the steady-state transport equation for nonthermal particles of species i:

$$\frac{d}{dE_i} \left( -\frac{E_i}{t_{i,\text{cool}}} N_{E_i} \right) = -\frac{N_{E_i}}{t_{\text{esc}}} + \dot{N}_{E_i},\tag{1}$$

where  $E_i$  is the particle energy (i = e or p),  $N_{E_i}$  is the total number spectrum,  $t_{i,\text{cool}}$  is the cooling time,  $t_{\text{esc}}$  is the escape time, and  $\dot{N}_{E_i}$  is the injection term. This equation has an analytic solution (see Appendix C in Dermer & Menon 2009):

$$N_{E_i} = \frac{t_{i,\text{cool}}}{E_i} \int_{E_i}^{\infty} dE_i' \dot{N}_{E_i'} \exp\left(-\int_{E_i}^{E_i'} \frac{t_{i,\text{cool}}}{t_{\text{esc}}} d\mathcal{E}_i\right). \tag{2}$$

We numerically integrate this equation to obtain the proton and electron spectra. We consider the diffusive shock acceleration mechanism at the knot and set the injection term to be a powerlaw form with an exponential cutoff:

$$\dot{N}_{E_i} = \dot{N}_{i,\text{nor}} \left( \frac{E_i}{E_{i,\text{cut}}} \right)^{-p_{\text{inj}}} \exp\left( -\frac{E_i}{E_{i,\text{cut}}} \right), \tag{3}$$

where  $\dot{N}_{i,\mathrm{nor}}$  is the normalization factor,  $p_{\mathrm{inj}}$  is the power-law index, and  $E_{i,\mathrm{cut}}$  is the cutoff energy determined by the balance between acceleration and loss timescales,  $t_{\mathrm{loss}}^{-1} = t_{\mathrm{cool}}^{-1} + t_{\mathrm{esc}}^{-1}$ . We normalize the normalization factor so that  $\int E_i \dot{N}_{E_i} dE_i = \varepsilon_i L_j$  is satisfied, where  $\varepsilon_i$  is the energy conversion factor.

We assume the same bulk velocity for the electrons and protons. They should have the same acceleration and diffusion timescales at a given energy. The diffusive shock acceleration time is given by

$$t_{\rm acc} \approx \frac{20\xi E_i}{3ceB\beta_i^2},\tag{4}$$

where  $\xi$  is the acceleration efficiency, B is the magnetic field strength, and  $\beta_j$  is the jet velocity. As the escape processes, we consider diffusion and advection, whose timescales are estimated to be

$$t_{\rm diff} pprox \frac{3eBR_{\rm knot}^2}{2c\xi E_i},$$
 (5)

$$t_{\rm adv} pprox rac{R_{
m knot}}{V_{
m adv}},$$
 (6)

where  $R_{\rm knot}$  is the size of the knot and  $V_{\rm adv}$  is the advection velocity at the knot. Assuming a spherical geometry of the emission region, the adiabatic cooling timescale is expressed as

$$t_{
m adi} pprox rac{R_{
m dis}}{V_{
m adv}},$$
 (7)

where  $R_{\rm dis}$  is the distance of the dissipation region from the central object. Note that if the jet geometry is cylindrical, one can ignore the adiabatic cooling (Sudoh et al. 2020).

For the electron radiation processes, we consider synchrotron and inverse Compton (IC) scattering. The synchrotron time-scale for the species i is represented as

$$t_{i,\text{syn}} pprox \frac{6\pi m_e^2 c^3}{\sigma_T B^2 E_i} \left(\frac{m_i}{m_e}\right)^2,$$
 (8)

where  $m_i$  is the mass of the particle i and  $\sigma_T$  is the Thomson cross section. We use a fitting formula (Equations (18)–(20) in Finke et al. 2008) to calculate the synchrotron spectrum. The IC cooling rate is estimated using Equation (2.56) in Blumenthal & Gould (1970), and the IC spectrum is calculated by Equation (2.48) in Blumenthal & Gould (1970). We consider only the cosmic microwave background (CMB) as the target photons, since IC emission using other photon fields is subdominant (Fang et al. 2020; Sudoh et al. 2020).

For the hadronic radiation processes, we consider only the pp inelastic collisions, because other processes are negligibly efficient (Reynoso & Carulli 2019). We should note that for  $n_{\rm eff} \lesssim 0.01$ , external photon fields by the central star or by the beamed emission from the inner jets may be important. The pp cooling rate is estimated to be

$$t_{pp}^{-1} = n_{\text{eff}} \sigma_{pp} \kappa_{pp} c, \tag{9}$$

where  $n_{\rm eff}$  is the effective number density (defined in the following subsection),  $\sigma_{pp}$  is the pp inelastic collision cross section given in Kafexhiu et al. (2014), and  $\kappa_{pp} \approx 0.17$  is the inelasticity for pp interaction (Kelner et al. 2006). We use the method of Kelner et al. (2006) to calculate the gamma-ray spectrum by pp inelastic collisions.

# 2.2. Model Parameters

Multiwavelength observations of SS 433 provide useful information to model the high-energy emission from the extended jets. The jet velocity is measured to be  $\beta_j \simeq 0.26$  at the jet base using both optical (Abell & Margon 1979; Eikenberry et al. 2001) and X-ray data (Marshall et al. 2002). The mass-loss rate of the jet is estimated to be  $\dot{M}_j \simeq 5 \times 10^{-7} \, M_{\odot} \, yr^{-1}$  (Konigl 1983), which leads to a kinetic energy of the jet of  $L_j \approx \dot{M} \beta_j^2 c^2/2 \simeq 2 \times 10^{39} \, {\rm erg \ s^{-1}}$ . The size and the distance from the central object for the brightest X-ray knot (e2)

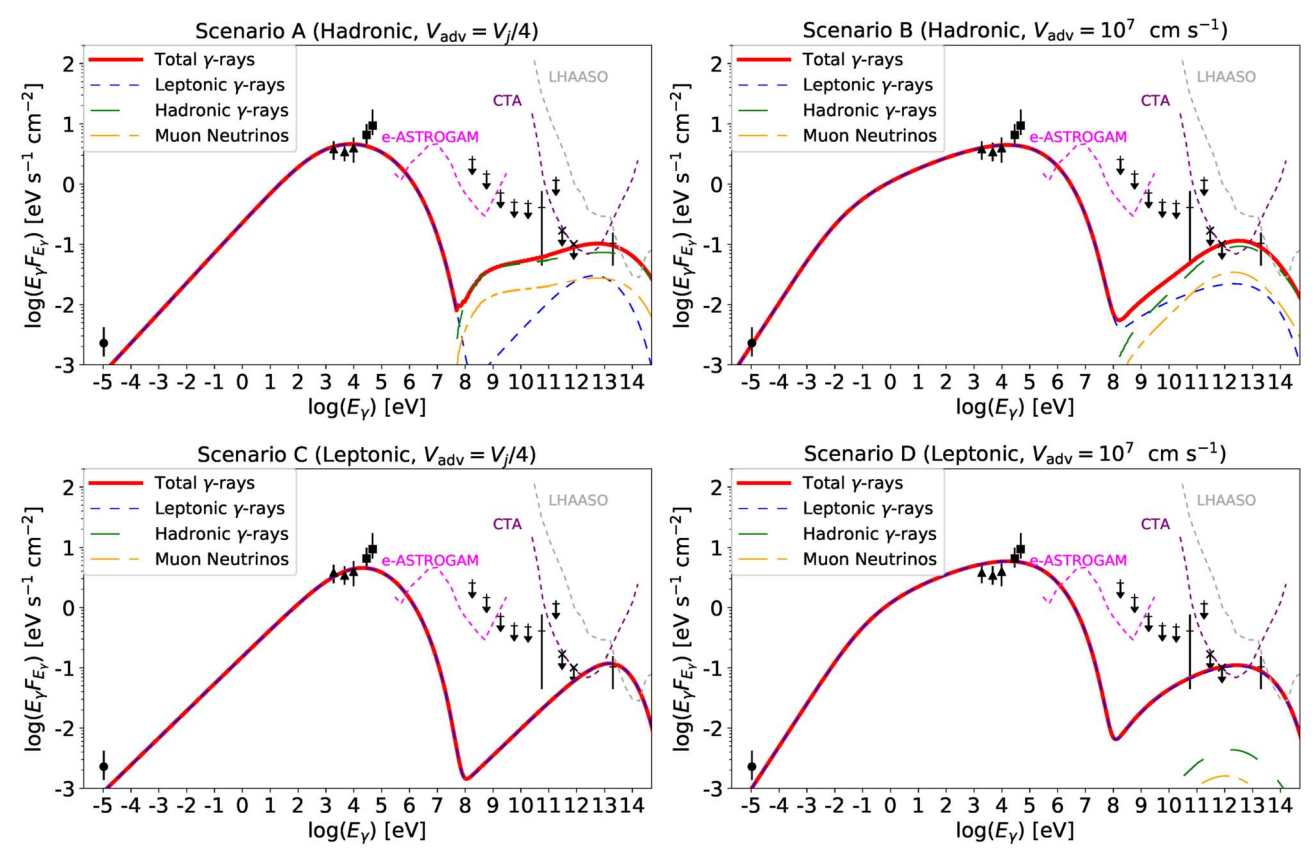


Figure 2. Photon spectra from the extended jets of SS 433 for scenario A (top left), B (top right), C (bottom left), and D (bottom right). The red thick solid, green thin long-dashed, and blue thin short-dashed lines are total, hadronic, and leptonic components, respectively. The observational data are taken from Geldzahler et al. (1980) (circle), Brinkmann et al. (2007) (triangles), Safi-Harb & Ögelman (1997) (squares), MAGIC Collaboration et al. (2018) (crosses), and Fang et al. (2020) (pluses). The thin solid, thin dashed, and thin dotted lines are sensitivity curves for e-ASTROGAM (1 yr; De Angelis et al. 2017), CTA (50 hr; Cherenkov Telescope Array Consortium et al. 2019), and LHAASO (1 yr; Bai et al. 2019). Scenarios A, B, and D can reproduce the GeV-TeV gamma-ray data, while scenario C cannot reproduce the Fermi data. The thin dotted-dashed lines are the muon neutrino spectra (i.e., neutrino spectra per flavor). Also, the CTA sensitivity curve is for a point source. The TeV gamma-ray emission region in SS 433 is extended, which worsens the sensitivity.

are 5' and 35', respectively (Safi-Harb & Ögelman 1997), which correspond to  $R_{\rm dis} \simeq 56$  pc and  $R_{\rm knot} \simeq 8.1$  pc, with a distance of  $d_L = 5.5$  kpc.

Optical observations discovered filamentary structures located close to the X-ray knots (Zealey et al. 1980), where the number density can be as high as  $n \sim 10^2 \, \mathrm{cm}^{-3}$  (Konigl 1983) and the velocity is estimated to be  $V_{\rm adv} \sim 10^7 \, {\rm cm \ s^{-1}}$  (Boumis et al. 2007). On the other hand, Panferov (2017) estimates the mean number density in W50 to be  $n \sim 0.1$  cm<sup>-3</sup>, and argues that the jet is not significantly decelerated at the X-ray knot. In this case, the bulk velocity of the emission region is likely to be  $V_{\rm adv} \approx \beta_j c/4$ , where the factor 4 indicates energy dissipation by a strong shock. Since the advection velocity and the target gas density in the X-ray knot are still largely uncertain, we examine two values of the advection velocity:  $V_{\rm adv}=\beta_j c/4\simeq 1.9 imes$  $10^9 \,\mathrm{cm} \,\mathrm{s}^{-1}$  (scenarios A and C) or  $V_{\mathrm{adv}} = 10^7 \,\mathrm{cm} \,\mathrm{s}^{-1}$  (scenarios B and D). Even for the low advection velocity cases, we assume a shock velocity of  $\beta_i$ , because the accelerated electrons cannot emit the observed X-rays with a lower value of the shock velocity (see Section 3). Regarding the number density, we define the effective number density as  $n_{\rm eff} = f_{\rm fil} \, n_{\rm fil}$ , where  $n_{\rm fil}\sim 100~{
m cm^{-3}}$  and  $f_{\rm fil}\sim 10^{-4}$ –1 are the number density and the volume filling factor of the optical filaments, respectively. Here we note that the magnetic field strength and the effective number density are treated as independent parameters. Also,

because we assume  $f_{\rm fil}\ll 1$  in our scenarios, we should evaluate the magnetic field strength at the X-ray knot, and the magnetic field strength does not have to scale with the effective density.

# 3. Results

We calculate the photon spectra for various values of  $p_{\rm inj}$ ,  $\varepsilon_e$ , B, and  $n_{\rm eff}$  to seek the parameter set that matches the data. Since the radio map of W50 does not indicate any clear knot-like structure (Dubner et al. 1998), we should regard the radio data as an upper limit. We match the data by eye inspection, and do not discuss the goodness of fit because of the observational uncertainty and the limitation of the models. Figure 2 shows both the leptonic and hadronic contributions to the photon spectra for our scenarios whose parameter sets are tabulated in Table 1. For all the scenarios, the electron synchrotron emission is responsible for the X-ray data. The Lorentz factor of electrons emitting the hard X-rays is estimated to be

$$\gamma_{e,X} \approx \sqrt{\frac{4\pi m_e c E_{\gamma}}{h_p e B}} \simeq 4.1 \times 10^8 B_{-4.5}^{-1/2} \left(\frac{E_{\gamma}}{30 \text{ keV}}\right)^{1/2}, \quad (10)$$

where  $h_p$  is the Planck constant. The synchrotron cooling is the dominant loss process in this energy range for all the scenarios.

Table 1

Model Parameters in Our Leptohadronic Scenarios; Scenarios A and B are Hadronic Dominated, while C and D are Leptonic Dominated

Fixed Parameters								
$\beta_j$	$L_j$ (erg s <sup>-1</sup> )	R <sub>knot</sub> (pc)	R <sub>dis</sub> (pc)	$\varepsilon_p$	ξ	d <sub>L</sub> (kpc)		
0.26	$2 \times 10^{39}$	8.1	56	0.1	2	5.5		
		Model	Parameter	rs				
Scenario	$V_{\rm adv}$ (cm s <sup>-1</sup> )	<i>B</i> (G)	$p_{ m inj}$	$\varepsilon_{\epsilon}$	?	$n_{\rm eff}$ (cm <sup>-3</sup> )		
A B C D	$1.9 \times 10^9$ $1.0 \times 10^7$ $1.9 \times 10^9$ $1.0 \times 10^7$	32 36 13 18	2.0 1.6 2.1 1.6	1.0 × 1.5 × 5.0 × 2.0 ×	$10^{-4}$ $10^{-3}$	10 0.2 0.01 0.01		

Equating the synchrotron and acceleration timescales, we obtain the maximum Lorentz factor of the electrons:

$$\gamma_{e,\text{cut}} \approx \sqrt{\frac{9\pi e \beta_j^2}{10\sigma_T B \xi}} \simeq 2.1 \times 10^9 B_{-4.5}^{-1/2} \xi_0^{-1/2}.$$
(11)

From the condition  $\gamma_{e,X} < \gamma_{e,\mathrm{cut}}$ , we obtain an upper limit for  $\eta$ :

$$\xi \approx \frac{9}{40} \frac{h_p e^2 \beta_j^2}{\sigma_T m_e c E_{\gamma}} \simeq 27 \left(\frac{E_{\gamma}}{30 \text{keV}}\right)^{-1}.$$
 (12)

Thus, the particle acceleration should be very efficient. The synchrotron cutoff feature should be detected by the proposed MeV satellites, such as e-ASTROGAM (De Angelis et al. 2017), All-sky Medium Energy Gamma-ray Observatory (AMEGO; Moiseev 2017), or Gamma-Ray and AntiMatter Survey (GRAMS; Aramaki et al. 2020), which will provide a better constraint on the value of  $\mathcal{E}$ .

The synchrotron-cooling break energies for photons and electrons are respectively estimated to be

$$E_{\gamma,\text{br}} \approx \frac{h_p e B \gamma_{e,\text{br}}^2}{4\pi m_e c} \simeq 0.70 B_{-4.5}^{-3} V_{\text{adv},9.3}^2 \text{ keV},$$
 (13)

$$\gamma_{e, \text{br}} \approx \frac{6\pi m_e c V_{\text{adv}}}{\sigma_T B^2 R_{\text{knot}}} \simeq 6.2 \times 10^7 B_{-4.5}^{-2} V_{\text{adv}, 9.3}.$$
(14)

The break energy lies between the radio and X-ray data points, and  $E_{\gamma, \rm br}$  is lower for a lower value of  $V_{\rm adv}$  and a higher value of  $V_{\rm adv}$  and a higher value of  $V_{\rm adv}$  and  $V_{\rm adv}$  and a higher value of  $V_{\rm adv}$  and  $V_{\rm adv}$  are scenarios A and C,  $V_{\rm inj}$  is consistent with the prediction by the diffusive shock acceleration theory (Bell 1978; Blandford & Ostriker 1978), whereas scenarios B and D demand a harder spectrum that can be realized by the stochastic acceleration mechanism (e.g., Becker et al. 2006; Stawarz & Petrosian 2008; Kimura et al. 2015; Murase et al. 2020).

As far as the hadronic components, the hadronic gamma-ray spectra roughly follow the parent proton spectra, which have a break due to the diffusive escape. Setting  $t_{\text{diff}} = t_{\text{adv}}$ , the proton

break energy is estimated to be

$$E_{p,\text{br}} \approx \frac{3eBR_{\text{knot}}V_{\text{adv}}}{2c\xi} \simeq 23B_{-4.5}V_{\text{adv},9.3}\xi_0^{-1} \text{ PeV}.$$
 (15)

For scenario A, the proton spectrum is a single power law for  $E_p \lesssim 0.1 \text{ PeV}$  owing to a higher break energy. This naturally makes a power-law gamma-ray spectrum consistent with the observed data. This feature should be detected by the Cherenkov Telescope Array (CTA; Cherenkov Telescope Array Consortium et al. 2019), the Large High-Altitude Air Shower Observatory (LHAASO; Bai et al. 2019), and the Southern Wide-field Gamma-ray Observatory (SWGO; Albert et al. 2019). The detection of a relatively hard sub-PeV gammaray spectrum is a smoking gun to distinguish the emission mechanism, because the IC upscattering of CMB photons cannot produce such a feature due to the Klein-Nishina suppression, as shown in the bottom panels of Figure 2. For scenario B, the diffusive break energy is  $E_{p,br} \simeq 60$  TeV. This produces a peak at  $E_{\gamma} \sim 6$  TeV, and the gamma-ray spectrum is softer above that energy. In this case, we cannot discriminate the emission mechanism using the gamma-ray spectrum. The proton maximum energy is determined by the diffusive escape in all the scenarios:

$$E_{p,\text{diff}} \approx \frac{3eB\beta_j R_{\text{knot}}}{\sqrt{40}\,\xi} \simeq 29B_{-4.5}\xi_0^{-1}\,\text{PeV}.$$
 (16)

This energy is so high that SS 433 can accelerate protons above PeV energies (see Section 5 for the possible effects of PeV protons).

For leptonic scenarios, the GeV–TeV gamma rays are attributed to IC upscattering. In scenario C, the high advection velocity makes the break energy too high to match the observation. This cannot make a flat spectrum in the GeV–TeV range, thus failing to explain the Fermi data, as in Sudoh et al. 2020. On the other hand, in scenario D, the advection time is comparable to the estimated age of the system (30–100 kyr). This enables us to reproduce the broadband spectrum owing to a lower cooling break energy. The resulting spectrum is similar to that by Fang et al. (2020).

In our scenario, the magnetic field is unlikely to be generated by some plasma instabilities. The magnetic field in the downstream is often estimated using the  $\varepsilon_B$  parameter to be

$$B = \sqrt{\frac{8\varepsilon_B L_j}{R_{\text{knot}}^2 \beta_j c}}.$$
 (17)

With our choice of B,  $\varepsilon_B$  is estimated to be 0.3, 0.4, 0.05, and 0.1 for scenarios A, B, C, and D, respectively. These values are much higher than the values obtained by PIC simulations of nonrelativistic shocks (Caprioli & Spitkovsky 2014; Park et al. 2015) and afterglow lightcurve fittings of gamma-ray bursts (Santana et al. 2014). In the leptonic scenario, the observed flux ratio of X-rays to TeV gamma rays requires the magnetic field strength of  $B \sim 15 \ \mu\text{G}$ , i.e.,  $\varepsilon_B \sim 0.1$  (Reynoso & Carulli 2019; Xing et al. 2019; Fang et al. 2020; Sudoh et al. 2020). In order for hadronic scenarios to work, a higher magnetic field strength is necessary, and hence  $\varepsilon_B \gtrsim 0.2$  is required. Note that magnetic fields in our models are not strong compared to that in the interstellar medium (ISM;  $B \sim 1-10 \ \mu\text{G}$ ). Shock

compression of the ISM field suffices to achieve the values, although it cannot generate the magnetic field of  $B > 40~\mu G$  for a typical ISM value,  $B_{\rm ISM} \sim 10~\mu G$ . Hence, the magnetic field should be in the range of 10–40  $\mu G$  regardless of the emission mechanism.

# 4. Comparison to Jets in Radio Galaxies

In our scenarios, the synchrotron-cooling timescales for X-ray emitting electrons are estimated to be  $t_{\rm syn} \simeq 78B_{-4.5}\gamma_{\rm e,8.5}$  yr. This is shorter than the advection timescale for all the scenarios,  $t_{\rm adv} \simeq 4.0 \times 10^2 V_{\rm adv,9.3}$  yr. This demands in situ particle acceleration in the extended jet with a low  $\xi$ . This situation may be similar to some of the extended jets in radio galaxies, where the in situ electron acceleration is required. In our assumption for the advection velocity, scenarios A and C correspond to the X-ray knot in radio galaxies because the jets are unlikely to be appreciably decelerated at the knots. On the other hand, scenarios B and D are similar to hot spots in radio galaxies, since the termination shock significantly decelerates the plasma flow and forms the cocoon surrounding the jets.

M87 and 3C 273 are very bright radio galaxies, and the broadband spectra and velocities of their knots are observed. For M87, the knots in the 10–100 pc scale have soft X-ray spectra without a cutoff feature (Zhang et al. 2018). Their intrinsic velocity is estimated to be  $\Gamma\beta\sim 0.3$ –10 with a possible velocity stratification (Park et al. 2019). On the other hand, for 3C 273, the X-ray spectra for the knots in the kiloparsec scale is hard, and nondetection by Fermi suggests a second electron population (Meyer & Georganopoulos 2014). Their apparent velocities are consistent with  $\beta_{\rm app}\sim 0$  (Meyer et al. 2017). For both objects, X-rays are attributed to the in situ accelerated electrons, which suggests a low value of  $\xi\lesssim 300$  based on Equation (12) with  $\beta_j\sim 0.3$ . On the other hand, the jet velocity may be very different in these objects, and hence the value of  $\xi$  should be independent of the jet velocity.

According to Zhang et al. (2018), the peak frequency of the synchrotron spectrum and the magnetic field strength in X-ray knots and hot spots in radio galaxies are estimated to be  $u_{\rm pk} \sim 10^9 \text{--} 10^{17} \text{ Hz} \text{ and } B \sim 10 \text{--} 300 \, \mu \text{ G, respectively. The}$ radio, optical, and X-ray spectra for some knots are inconsistent with a single component synchrotron emission. A popular interpretation of the emission mechanism for the X-ray emission from the knots is inverse Compton scattering of CMB photons (IC/CMB model; Tavecchio et al. 2000; Sambruna et al. 2004; Werner et al. 2012). However, nondetection of GeV gamma-rays by Fermi-LAT ruled out an IC/CMB model for several sources (e.g., Breiding et al. 2017). The two-component synchrotron model is favored as an alternative scenario for those sources (Atoyan & Dermer 2004), which indicates a low value of  $\xi$  as in M87 and 3C 273. The shock velocities at the hot spots or X-ray knots are often assumed to be 0.2c-0.5c (Casse & Marcowith 2005), which is also supported by the radio observations of kiloparsec-scale jets (Wardle & Aaron 1997; Arshakian & Longair 2004; Mullin & Hardcastle 2009). Hence, some X-ray knots in radio galaxies should have a very low  $\xi$ , which is consistent with our SS 433 models.

If protons are accelerated at the X-ray knots simultaneously, the maximum energy of the protons is estimated to be  $E_{p,\mathrm{diff}} \sim 45 B_{-4.5} \xi_0^{-1} \beta_{j,-0.5} R_{j,22.5}$  EeV. The iron nuclei can be accelerated up to 26 times higher energies than protons, and hence the kiloparsec-scale jets in radio galaxies can accelerate

heavy nuclei to ultrahigh energies (see also Takahara 1990). However, reproducing the heavy composition obtained by the Pierre Auger Observatory (Aab et al. 2014) is challenging by the standard shock acceleration, and reacceleration of galactic cosmic rays (CRs) by jets may be important (Caprioli 2015; Kimura et al. 2018).

We should note that the value of  $\xi$  should be much higher at hot spots in radio galaxies and blazar zones. The cutoff frequency in the hot spots are estimated to be below the UV range,  $\nu_{\rm cut} \lesssim 10^{15}$  Hz, leading to  $\xi \gtrsim 10^4$  (Araudo et al. 2016; Zhang et al. 2018). Also, the IC/CMB model is still favored for some X-ray knots (Zhang et al. 2018), resulting in  $\xi$  similar to those in the hot spots. Fittings of the broadband spectra for blazars require  $\xi \gtrsim 10^4$  (Inoue & Takahara 1996; Inoue & Tanaka 2016; Baring et al. 2017). These may indicate that different particle acceleration mechanisms take place at the various places in the astrophysical jets.

#### 5. Discussion

### 5.1. Neutrino Detectability

Hadronic TeV gamma rays must be accompanied by neutrinos of similar energies and fluxes. The eastern lobe of SS 433 is located at the decl. of  $\delta = +4.9$ , so it is also an interesting target for IceCube and IceCube-Gen2. When the neutrino mixing is assumed, the ratio of pionic gamma rays to muon neutrinos is approximately 2:1 when the main neutrino production channel is the inelastic pp reaction (e.g., Murase et al. 2013, and references therein). Indeed, in scenarios A and B, the predicted neutrino fluxes are  $\sim 3 \times 10^{-11} \, \text{GeV cm}^{-2} \, \text{s}^{-1}$ in the 10-100 TeV range, which is lower than IceCube's 10 year sensitivity of  $\sim 3 \times 10^{-10}\,\mathrm{GeV}\,\mathrm{cm}^{-2}\,\mathrm{s}^{-1}$  for an  $E_{\nu}^{-2}$  spectrum (Aartsen et al. 2020). The next-generation detector IceCube-Gen2 will have about 5 times better sensitivity than IceCube (The IceCube-Gen2 Collaboration et al. 2020). Although the point-source neutrino detection of SS 433 would still be challenging, it might be possible with more than 2 decades of the observations by IceCube-Gen2, or joint analyses with HAWC-like detectors would be useful. If the proton spectrum is harder, the neutrino detection can be more promising. However, in such a case, the gamma-ray model spectrum would become inconsistent with the Fermi-LAT data and the existing upper limits by HESS/MAGIC. Using the HAWC data and the HESS/MAGIC upper limit, Reynoso & Carulli (2019) reached a similar conclusion, arguing that detectable neutrinos could be emitted from the inner region.

# 5.2. Particle Acceleration Efficiency in Other Objects

The SS 433 jets have a low  $\xi$ , while jets in radio galaxies may have various values of  $\xi$ . Other CR accelerators generally have low values of  $\xi$ . Sharp X-ray images are observed from the forward shocks in supernova remnants (SNRs; Bamba et al. 2005). The cutoff frequencies in SNRs are  $10^{17}$ – $10^{18}$  Hz, and shock velocities are  $\sim 2000-10^4$  km s<sup>-1</sup> (Reynolds 2008). These values require  $\xi \sim 1$ , according to Equation (12). Also, fittings of pulsar wind nebulae (PWNe) demand a very efficient particle acceleration of  $\xi \sim 1$  (Tanaka & Takahara 2011, 2013).

There are a few possible reasons for such distinct values of  $\xi$ . To achieve a high value of  $\xi$ , strong turbulence should exist. A possible mechanism generating turbulence is density perturbations in the upstream of the shocks. The ISM in our Galaxy has strong density perturbations, which can drive strong turbulence

when shocks sweep up the ISM (Inoue et al. 2012; Tomita et al. 2019). The hot spots and the blazar emission regions can arise at the reverse shocks in expanding jets, which likely have weaker density perturbations due to adiabatic expansion. Another possibility is related to the plasma composition. Magnetized ion–electron plasmas result in strong turbulence owing to the streaming instability (Skilling 1975; Bell 2004), whereas electron–positron pair plasmas may not trigger it. However, PWNe likely accelerate particles at reverse shocks and consist of pair plasmas, and neither of the interpretations are applicable. Further studies are necessary on both the theoretical and observational sides to understand the dichotomy of the acceleration efficiency.

# 5.3. Effects of Escaping CRs

In our hadronic scenarios, the protons of PeV energies escape from the system and are injected into the ISM. The diffusion coefficient in the ISM is often estimated by the boron-to-carbon ratio to be  $D_{\rm ISM}\approx 3\times 10^{30}E_{p,\,\rm PeV}^{1/3}\,{\rm cm^2~s^{-1}}$ , where  $E_{p,\rm PeV}=E_p/(1~{\rm PeV})$ , and we consider the Kolmogorov turbulence (Strong et al. 2007). Then, the diffusion length during the lifetime of SS 433,  $t_{\rm age}$ , is estimated to be

$$R_{\rm diff} \approx \sqrt{6D_{\rm ISM}t_{\rm age}} \simeq 1.4 E_{p, \rm PeV}^{1/6} t_{\rm age, 12}^{1/2} {\rm kpc.}$$
 (18)

Since  $R_{\text{diff}}$  is shorter than the distance to the Earth, the CRs escaping from SS 433 have not arrived at Earth yet. The energy density of the escaping CRs at the PeV energy is estimated to be

$$U_{\text{CR,PeV}} \approx \frac{3\varepsilon_p L_j t_{\text{age}} f_{\text{bol}}}{4\pi R_{\text{diff}}^3}$$
$$\sim 3 \times 10^{-5} \varepsilon_{p,-1} L_{j,39.3} t_{\text{age},12}^{-1/2} E_{p,\text{PeV}}^{-1} \text{ eV cm}^{-3}, \tag{19}$$

where the factor  $f_{\rm bol}\approx 1/\ln(E_{p,\rm max}/{\rm GeV})\sim 1/15$  is the bolometric correction factor. The recent observations by Telescope Array Low-energy Extension (TALE) and IceTop reported that the CR energy density at the PeV energy is  $\sim 1\times 10^{-4}~{\rm eV}~{\rm cm}^{-3}$  (Abbasi et al. 2018; Aartsen et al. 2019), which matches the estimate above within an order of magnitude. Hence, Galactic X-ray binaries may provide some contribution to the PeV CRs (see Cooper et al. 2020). The lifetime of SS 433 may be longer,  $t_{\rm age}\sim 10^5-10^6~{\rm yr}$  (Yamamoto et al. 2008; Su et al. 2018), and the escaping CRs can arrive at Earth if we use  $t_{\rm age}=10^6~{\rm yr}$ . In this case, SS 433 can contribute to the observed PeV CRs up to 6%.

#### 5.4. Comparison to Previous Work

Previous studies on TeV gamma-ray emission from SS 433 mainly discussed the leptonic scenarios (Abeysekara et al. 2018; Xing et al. 2019; Sudoh et al. 2020). Our leptonic scenarios C and D are similar to the models by Sudoh et al. (2020) and Abeysekara et al. (2018), respectively. However, we find that scenario C cannot reproduce the latest Fermi data by Fang et al. (2020), although the GeV detection is not significant enough by the Fermi data alone. On the other hand, scenario D can reproduce the Fermi data as argued in Fang et al. (2020).

The previous literature concluded that the hadronic scenarios are disfavored because the required jet power is too high for a typical number density of  $\sim 0.01$ – $0.1~\rm cm^{-3}$  in the W50 nebula

 Table 2

 Consistency Check for Our Scenarios

Scenario	На	adronic	Leptonic	
	A Knot	B Hot Spot	C Knot	D Hot Spot
HAWC data	О	О	О	0
Fermi data	O	O	X	O
Ambient density	$\Delta$	O	O	O
AGN analog	O	X	O	X

**Note.** Here "AGN analog" indicates whether the value of  $\xi$  in our scenario is consistent with those obtained from the radio galaxies' X-ray knots. O,  $\Delta$ , and X indicate consistent, marginal, and inconsistent, respectively.

(Abeysekara et al. 2018; Sudoh et al. 2020). However, their conclusions were obtained without examining the effect of optical filaments, where the density can be much higher. A higher number density enables our hadronic scenario to naturally reproduce the GeV–TeV gamma-ray data with a reasonable jet power. Therefore, we conclude that both leptonic and hadronic scenarios can reproduce the GeV–TeV gamma-ray data.

# 6. Summary

We examined both leptonic and hadronic scenarios for GeV-TeV gamma-ray emission from the SS 433 jets in light of the recent detections by Fermi and HAWC. The gamma-ray emission region coincides with the X-ray knots and the optical filaments, where particle acceleration should be efficient and the target density should be high, respectively. To obtain broadband photon spectra, we solved the transport equations for electrons and protons taking into account acceleration, radiative and adiabatic cooling, and diffusive and advective escape. Fixing several parameters based on the multiwavelength observations of the SS 433/W50 system, we searched parameter sets with which the resulting photon spectra match the observed data. We found that both hadronic and leptonic scenarios can reproduce the observed data without violating current observational constraints. The radio to X-ray data are emitted by electron synchrotron radiation and the GeV-TeV gamma rays are produced by either the pion decay process or IC emission. The spectral shapes strongly depend on the advection timescale, and future observations by CTA, LHAASO, and SWGO will provide more clues to distinguish between the scenarios.

Finally, we summarize the feasibility of our scenarios in terms of the gamma-ray spectrum, the ambient number density, and analogy to large-scale AGN jets (see Table 2). Scenarios A, B, and D can reproduce the GeV-TeV gamma-ray data, while scenario C cannot reproduce the Fermi data. The estimates of the ambient density in the W50 region prefer  $n_{\rm eff} \sim 0.01$ –0.1 cm<sup>-3</sup> (Safi-Harb & Petre 1999; Panferov 2017), which is consistent with scenarios B, C, and D. However, the density in the optical filaments is as high as 100 cm<sup>-3</sup>, and the filling factor of the filaments is unclear from observations. Thus, a value for scenario A of  $n_{\rm eff} \sim 10~{\rm cm}^{-3}$  is also acceptable. In the large-scale jets of radio galaxies, the knots and hot spots have low and high values of  $\xi$ , respectively. Our scenarios assume a low value of  $\xi$ , which corresponds to the values in knots where the advection velocity is high, making scenarios A and C suitable. Therefore, in this regard, we conclude that our hadronic scenario A would be the most plausible scenario for the high-energy gamma-ray emission

mechanism of SS 433. If the same mechanism operates in radio galaxies this implies that the X-ray knot region of the jets in radio galaxies may accelerate heavy nuclei up to ultrahigh energies. To more solidly understand the emission mechanisms in these objects, further investigations from both the observational and theoretical sides are necessary. In particular, future MeV gamma-ray observations will clarify the value of  $\xi$  and observations of >100 TeV photons by LHAASSO, SWGO, or CTA may be able to discriminate between the scenarios.

We thank Ke Fang, Takahiro Sudoh, and Kenji Toma for useful discussion. This work is partly supported by JSPS Research Fellowship, KAKENHI No. 19J00198 (S.S.K.), and the Alfred P. Sloan Foundation, NSF grant No. AST-1908689, and KAKENHI No. 20H01901 (K.M.), and the Eberly Foundation (P.M.).

### ORCID iDs

Shigeo S. Kimura https://orcid.org/0000-0003-2579-7266 Kohta Murase https://orcid.org/0000-0002-5358-5642 Peter Mészáros https://orcid.org/0000-0002-4132-1746

#### References

```
Aab, A., Abreu, P., Aglietta, M., et al. 2014, PhRvD, 90, 122005
Aartsen, M. G., Ackermann, M., Adams, J., et al. 2019, PhRvD, 100, 082002
Aartsen, M. G., Ackermann, M., Adams, J., et al. 2020, PhRvL, 124, 051103
Abbasi, R. U., Abe, M., Abu-Zayyad, T., et al. 2018, ApJ, 865, 74
Abdollahi, S., Acero, F., Ackermann, M., et al. 2020, ApJS, 247, 33
Abell, G. O., & Margon, B. 1979, Natur, 279, 701
Abeysekara, A. U., Albert, A., Alfaro, R., et al. 2018, Natur, 562, 82
Albert, A., Alfaro, R., Ashkar, H., et al. 2019, arXiv:1902.08429
Aramaki, T., Adrian, P. O. H., Karagiorgi, G., & Odaka, H. 2020, APh,
   114, 107
Araudo, A. T., Bell, A. R., Crilly, A., & Blundell, K. M. 2016, MNRAS,
   460, 3554
Arshakian, T. G., & Longair, M. S. 2004, MNRAS, 351, 727
Atoyan, A., & Dermer, C. D. 2004, ApJ, 613, 151
Bai, X., Bi, B. Y., Bi, X. J., et al. 2019, arXiv:1905.02773
Bamba, A., Yamazaki, R., Yoshida, T., Terasawa, T., & Koyama, K. 2005,
   ApJ, 621, 793
Baring, M. G., Böttcher, M., & Summerlin, E. J. 2017, MNRAS, 464, 4875
Becker, P. A., Le, T., & Dermer, C. D. 2006, ApJ, 647, 539
Bell, A. R. 1978, MNRAS, 182, 147
Bell, A. R. 2004, MNRAS, 353, 550
Blandford, R. D., & Ostriker, J. P. 1978, ApJL, 221, L29
Blumenthal, G. R., & Gould, R. J. 1970, RvMP, 42, 237
Bordas, P., Yang, R., Kafexhiu, E., & Aharonian, F. 2015, ApJL, 807, L8
Boumis, P., Meaburn, J., Alikakos, J., et al. 2007, MNRAS, 381, 308
Breiding, P., Meyer, E. T., Georganopoulos, M., et al. 2017, ApJ, 849, 95
Brinkmann, W., Pratt, G. W., Rohr, S., Kawai, N., & Burwitz, V. 2007, A&A,
  463, 611
Caprioli, D. 2015, ApJL, 811, L38
Caprioli, D., & Spitkovsky, A. 2014, ApJ, 794, 46
Casse, F., & Marcowith, A. 2005, APh, 23, 31
Cherenkov Telescope Array Consortium, Acharya, B. S., Agudo, I., et al. 2019,
   Science with the Cherenkov Telescope Array (Singapore: World Scientific )
Cooper, A. J., Gaggero, D., Markoff, S., & Zhang, S. 2020, MNRAS,
   493, 3212
```

```
De Angelis, A., Tatischeff, V., Tavani, M., et al. 2017, ExA, 44, 25
Dermer, C. D., & Menon, G. 2009, High Energy Radiation from Black Holes:
  Gamma Rays, Cosmic Rays, and Neutrinos (Princeton, NJ: Princeton Univ.
Dubner, G. M., Holdaway, M., Goss, W. M., & Mirabel, I. F. 1998, AJ,
   116, 1842
Eikenberry, S. S., Cameron, P. B., Fierce, B. W., et al. 2001, ApJ, 561, 1027
Fabrika, S. 2004, ASPRv, 12, 1
Fang, K., Charles, E., & Blandford, R. D. 2020, ApJL, 889, L5
Finke, J. D., Dermer, C. D., & Böttcher, M. 2008, ApJ, 686, 181
Geldzahler, B. J., Pauls, T., & Salter, C. J. 1980, A&A, 84, 237
Inoue, S., & Takahara, F. 1996, ApJ, 463, 555
Inoue, T., Yamazaki, R., Inutsuka, S.-I., & Fukui, Y. 2012, ApJ, 744, 71
Inoue, Y., & Tanaka, Y. T. 2016, ApJ, 828, 13
Kafexhiu, E., Aharonian, F., Taylor, A. M., & Vila, G. S. 2014, PhRvD, 90,
   123014
Kelner, S. R., Aharonian, F. A., & Bugayov, V. V. 2006, PhRvD, 74, 034018
Kimura, S. S., Murase, K., & Toma, K. 2015, ApJ, 806, 159
Kimura, S. S., Murase, K., & Zhang, B. T. 2018, PhRvD, 97, 023026
Konigl, A. 1983, MNRAS, 205, 471
MAGIC Collaboration, Ahnen, M. L., Ansoldi, S., et al. 2018, A&A, 612, A14
Marshall, H. L., Canizares, C. R., & Schulz, N. S. 2002, ApJ, 564, 941
Meyer, E., Sparks, W., Georganopoulos, M., et al. 2017, Galax, 5, 8
Meyer, E. T., & Georganopoulos, M. 2014, ApJL, 780, L27
Moiseev, A. 2017, ICRC (Busan), 301, 798
Mullin, L. M., & Hardcastle, M. J. 2009, MNRAS, 398, 1989
Murase, K., Ahlers, M., & Lacki, B. C. 2013, PhRvD, 88, 121301
Murase, K., Kimura, S. S., & Mészáros, P. 2020, PhRvL, 125, 011101
Panferov, A. A. 2017, A&A, 599, A77
Park, J., Caprioli, D., & Spitkovsky, A. 2015, PhRvL, 114, 085003
Park, J., Hada, K., Kino, M., et al. 2019, ApJ, 887, 147
Rasul, K., Chadwick, P. M., Graham, J. A., & Brown, A. M. 2019, MNRAS,
  485, 2970
Reynolds, S. P. 2008, ARA&A, 46, 89
Reynoso, M. M., & Carulli, A. M. 2019, APh, 109, 25
Safi-Harb, S., & Ögelman, H. 1997, ApJ, 483, 868
Safi-Harb, S., & Petre, R. 1999, ApJ, 512, 784
Sambruna, R. M., Gambill, J. K., Maraschi, L., et al. 2004, ApJ, 608, 698
Santana, R., Barniol Duran, R., & Kumar, P. 2014, ApJ, 785, 29
Seward, F., Grindlay, J., Seaquist, E., & Gilmore, W. 1980, Natur, 287, 806
Skilling, J. 1975, MNRAS, 173, 255
Stawarz, Ł., & Petrosian, V. 2008, ApJ, 681, 1725
Strong, A. W., Moskalenko, I. V., & Ptuskin, V. S. 2007, ARNPS, 57, 285
Su, Y., Zhou, X., Yang, J., et al. 2018, ApJ, 863, 103
Sudoh, T., Inoue, Y., & Khangulyan, D. 2020, ApJ, 889, 146
Sun, X.-N., Yang, R.-Z., Liu, B., Xi, S.-Q., & Wang, X.-Y. 2019, A&A,
  626, A113
Takahara, F. 1990, PThPh, 83, 1071
Tanaka, S. J., & Takahara, F. 2011, ApJ, 741, 40
Tanaka, S. J., & Takahara, F. 2013, MNRAS, 429, 2945
Tavecchio, F., Maraschi, L., Sambruna, R. M., & Urry, C. M. 2000, ApJL,
  544, L23
The IceCube-Gen2 Collaboration, Aartsen, M. G., Abbasi, R., et al. 2020,
  arXiv:2008.04323
Tomita, S., Ohira, Y., & Yamazaki, R. 2019, ApJ, 886, 54
van den Heuvel, E. P. J. 1981, VA, 25, 95
Wardle, J. F. C., & Aaron, S. E. 1997, MNRAS, 286, 425
Watson, M. G., Willingale, R., Grindlay, J. E., & Seward, F. D. 1983, ApJ,
Werner, M. W., Murphy, D. W., Livingston, J. H., et al. 2012, ApJ, 759, 86
Xing, Y., Wang, Z., Zhang, X., Chen, Y., & Jithesh, V. 2019, ApJ, 872, 25
Yamamoto, H., Ito, S., Ishigami, S., et al. 2008, PASJ, 60, 715
Yamauchi, S., Kawai, N., & Aoki, T. 1994, PASJ, 46, L109
Zealey, W. J., Dopita, M. A., & Malin, D. F. 1980, MNRAS, 192, 731
Zhang, J., Du, S.-S., Guo, S.-C., et al. 2018, ApJ, 858, 27
```